

## NO ENHANCEMENT OF LYMAN ALPHA EMITTERS IN QSO ENVIRONMENTS AT $Z \sim 4$ .<sup>\*</sup>

CRISTINA GARCÍA-VERGARA<sup>1,2</sup>, JOSEPH F. HENNAWI<sup>2,3</sup>, AND L. FELIPE BARRIENTOS<sup>1</sup>

*Draft version March 9, 2017*

### ABSTRACT

*Keywords:* cosmology: observations – early Universe – large-scale structure of Universe – galaxies: clusters: general – galaxies: high-redshift – quasars: general

### 1. INTRODUCTION

Throughout this paper, magnitudes are given in the AB system (Oke 1974; Fukugita et al. 1995) and we adopt a cosmology with  $H_0 = 70 \text{ km s}^{-1} \text{ Mpc}^{-1}$ ,  $\Omega_m = 0.26$  and  $\Omega_\Lambda = 0.74$ . We have adopted “cMpc” notation to refer to comoving units and “pkpc” to refer to proper units.

### 2. OBSERVATIONS AND DATA REDUCTION

LAEs are galaxies with a strong Lyman alpha emission line in their spectra. For the LAEs selection a NB filter is located just over the Ly $\alpha$  line and a broad band filter over the continuum. If the galaxy has a strong emission line, then it is expected to detect a flux excess in the narrow band filter compared with the broad band filter. Additionally, a second broad band filter is usually located blueward of the Ly $\alpha$  line, in order to detect the Lyman break due to the neutral hydrogen absorption by the IGM.

In this section, we provide detailed description about the QSO target selection, observations, and photometry performed to efficiently select LAEs at high redshift.

#### 2.1. Targeted QSO Fields and Observations

For this study, we observed 17 QSO fields using a NB with central wavelength at  $\lambda = 5930\text{\AA}$ . We have chosen this NB to identify LAEs at  $z \sim 3.87$  associated with the central QSO. We thus selected QSOs from the SDSS/BOSS QSO catalog in such a way that Ly $\alpha$  lands within the core of our filter at  $z \sim 3.87$ . Since we have stacked the LAEs counts from all the fields to measure clustering, it is important to select QSOs with an accurate redshift determination and a spanning of a very narrow redshift slice.

QSO redshifts are determined using a custom line-centering code that corrects the known relative shifts between broad rest-frame UV emission lines, and are accurate up to 800km/s, which is much narrower than the narrow band filter width ( $\sim 3200\text{km/s}$ ). Further, we selected only targets falling inside of the central 1000km/s of the NB filter in order to ensure that LAEs selected

with this band are associated to the central QSO in each field.

We just selected QSOs without radio emission counterpart reported in the the VLA FIRST catalog, since radio emission could affect environments. We also discarded QSOs with high extinctions ( $A_\lambda > 0.2$ ). Finally, we selected the brightest QSOs, to ensure they have massive black holes. Our final sample is composed by QSOs in a thin redshift slice of  $\Delta z \sim 0.02$  and with bright magnitudes  $i < 20.6$ . A summary of the QSOs properties are shown in the table 1.

Imaging observations for the sample of 17 QSO fields were carried out using the FOcal Reducer and low dispersion Spectrograph 2 (FORS2, Appenzeller & Rupprecht 1992) instrument on the Very Large Telescope (VLT) in 19 different nights between September, 2014 and March, 2015. The Field of View (FoV) of FORS2 is  $6.8 \times 6.8 \text{ arcmin}^2$  which corresponds to  $\sim 3.0 \times 3.0 \text{ pMpc}^2$  at  $z = 3.87$ . We used a  $2 \times 2$  binning readout mode, which results in an image pixel scale of 0.25 arcsec/pix. Each QSO field was observed using the NB HeI/2500+54 ( $\lambda = 5930\text{\AA}$ , FWHM = 63 $\text{\AA}$ , hereafter HeI) and the broad bands  $g_{\text{HIGH}}$  ( $\lambda = 4666\text{\AA}$ , hereafter  $g$ ) and  $R_{\text{SPECIAL}}$  ( $\lambda = 6522\text{\AA}$ , hereafter  $R$ ) in order to detect LAEs at  $z \sim 3.87$  (see Fig. 1).

The total exposure time per target for HeI,  $R$ , and  $g$  was 3660s, 360s, and 900s respectively, which was observed in shorter separated exposures in a dithered mode in order to fill the gap between the CCDs and to facilitate the reduction process (cosmic rays and bad pixel rejection, superflat building, etc). Note that these shorter exposures were not necessarily observed over the same night. The seeing during the 19 nights cover a range of 0.6 - 1.5 arcsec.

Spectrophotometric stars from different catalogs (???) were observed each night to calibrate the HeI and  $g$  images, and photometric standard stars from Stetson fields (Stetson 2000) were observed several times during the course of the night for the  $R$  images calibration. In the case of 2 nights none standard star was observed for the calibration of the  $g$  images, then in those cases we used the SDSS photometric catalogs to perform the flux calibration (these correspond to the fields SDSSJ0850 and SDSSJ1211).

#### 2.2. Data Reduction and Photometry

We performed the data reduction using standard IRAF<sup>5</sup> tasks and our own custom codes written in the

Electronic address: cgarcia@astro.puc.cl

<sup>\*</sup> Based on observations collected at the European Organization for Astronomical Research in the Southern Hemisphere, Chile. Data obtained from the ESO Archive, Normal program, service mode. Program ID: 094.A-0900.

<sup>1</sup> Instituto de Astrofísica, Pontificia Universidad Católica de Chile, Avenida Vicuña Mackenna 4860, Santiago, Chile.

<sup>2</sup> Max-Planck Institut für Astronomie (MPIA), Königstuhl 17, D-69117 Heidelberg, Germany.

<sup>3</sup> Department of Physics, University of California, Santa Barbara, CA 93106, USA

<sup>5</sup> Image Reduction and Analysis Facility

**Table 1**  
Targeted QSO properties.

Field	RA (J2000)	DEC (J2000)	Redshift	$i$
SDSSJ0040	00:40:17.426	+17:06:19.78	3.873	18.91
SDSSJ0042	00:42:19.748	-10:20:09.53	3.865	18.57
SDSSJ0047	00:47:30.356	+04:23:04.73	3.864	19.94
SDSSJ0119	01:19:59.553	-03:42:16.51	3.873	20.49
SDSSJ0149	01:49:06.960	-05:52:18.85	3.866	19.80
SDSSJ0202	02:02:53.765	-06:50:44.54	3.876	20.64
SDSSJ0240	02:40:33.804	+03:57:01.59	3.872	20.03
SDSSJ0850	08:50:13.457	+06:29:46.91	3.875	20.40
SDSSJ1026	10:26:32.976	+03:29:50.63	3.878	19.74
SDSSJ1044	10:44:27.798	+09:50:47.98	3.862	20.52
SDSSJ1138	11:38:05.242	+13:03:32.61	3.868	19.10
SDSSJ1205	12:05:39.550	+01:43:56.52	3.867	19.37
SDSSJ1211	12:11:46.935	+12:24:19.08	3.862	19.97
SDSSJ1224	12:24:20.658	+07:46:56.33	3.867	19.08
SDSSJ1258	12:58:42.118	-01:30:22.75	3.862	19.58
SDSSJ2250	22:50:52.659	-08:46:00.22	3.869	19.44
SDSSJ2350	23:50:32.306	+00:25:17.23	3.876	20.61

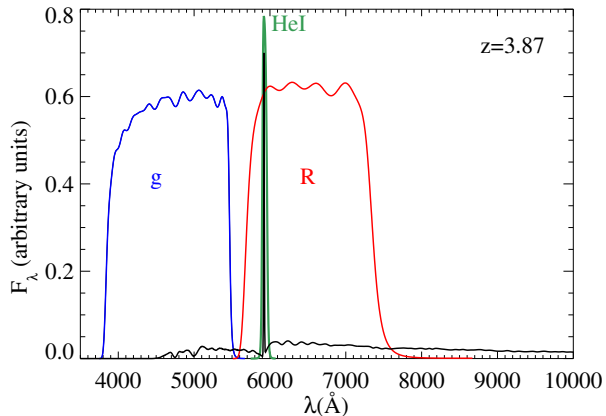


**Figure 1.** Filter configuration shown on a galaxy simulated spectra at  $z \sim 3.87$ .

Interactive Data Language (IDL) programming language. The reduction process included bias subtraction and flat fielding, which was performed using superflats images, created using the unregistered science frames. This allowed us to obtain a better reduced data without illumination patterns which were present if masterflats were used.

Given that the individual frames per filter could have been observed in different nights, the photometric calibration was done before the stacking process. For the case of *HeI* and *g* images, we had observed spectrophotometric stars, then we computed the star magnitude by convolving the filter transmission curves with the spectra. Then we compared this magnitude with the instrumental magnitudes obtained using SExtractor (Bertin & Arnouts 1996) on the science images, and then we compute the zeropoint (ZP) for the night in both bands. In the case of *R* images, we calibrated them comparing the tabulated standard stars magnitudes from the Stetson fields, with instrumental magnitudes measured on the science images, after correcting the tabulated magnitudes by the color term to take into account the difference between the Stetson and FORS2 *R* filter curve. We used all

the photometric stars of the field, and then we computed a median value for the final ZP. In the case of 2 nights were standard stars were not observed in *g*, we used the SDSS photometric catalogs to perform the photometric calibration. We compared the SDSS *g* magnitudes of some stars in the field with the instrumental magnitude of them measured on our science images, and then we computed the ZP for those nights.

We calibrate all our science images using their respective ZPs, and then we corrected them by airmass, using the atmospheric extinction curve over Cerro Paranal (Patat et al. 2011), and by galactic extinction calculated using the Schlegel dust maps (Schlegel et al. 1998) and extinction laws of Cardelli et al. (1989) with  $R_V = 3.1$ .

SExtractor and SCAMP (Bertin 2006) were used to detect sources on each individual calibrated image and to compute astrometric solution of it, using SDSS-DR9 r-band catalogs as the astrometric reference. Finally, the individual images were sky-subtracted, re-sampled and median-combined using SWarp (Bertin et al. 2002). The noisy edges of the combined images were cut and the bright stars were masked in order to avoid wrong objects detection due to star flux contamination.

Object detection and photometry were performed using SExtractor. Since we are interested in detection of LAEs, which have a strong Ly $\alpha$  line located in the core of the HeI NB, we used this image to detect objects, and then we performed photometry on the broad bands in the same positions an apertures. The background was calculated in regions of 64 pixels in size, and then recomputed locally in an annulus area of 24 pixels of thickness centered around the object. In order to maximize the detection of faint sources, the detection image was smoothed by applying a Gaussian filter of seeing FWHM of 2 pixels and size  $3 \times 3$  pixels. Every group of at least 7 contiguous pixels having a value above  $1.8\sigma$ , was defined as an object. Those parameters were chosen after iterating with different values and checking how many spurious object were detected, computed as in Hennawi et al. (2015).

We estimated the objects magnitudes using aperture photometry after convolving the images with a Gaussian kernel to match the seeing value. The magnitudes were measured in a fix aperture of  $2''$  of diameter. Magni-

**Table 2**  
 $5\sigma$  limit magnitudes per field  
measured in a  $2''$  diameter aperture.

Field	HeI	$g$	$R$
SDSSJ0040	25.14	26.28	25.43
SDSSJ0042	25.11	26.33	25.40
SDSSJ0047	24.77	26.14	25.45
SDSSJ0119	25.10	26.43	25.36
SDSSJ0149	25.20	26.47	25.39
SDSSJ0202	25.10	26.35	25.42
SDSSJ0240	24.83	25.93	25.44
SDSSJ0850	25.12	26.25	25.41
SDSSJ1026	25.29	26.39	25.25
SDSSJ1044	25.26	26.44	25.41
SDSSJ1138	24.69	25.83	25.11
SDSSJ1205	25.21	26.41	25.52
SDSSJ1211	25.16	26.25	25.12
SDSSJ1224	25.20	26.24	25.12
SDSSJ1258	25.15	26.38	25.44
SDSSJ2250	25.28	26.40	25.40
SDSSJ2350	25.14	26.19	25.37

tudes of objects not detected or detected with a signal to noise lower than 2 either in  $g$  or  $R$  were replaced by the corresponding  $2\sigma$  limiting magnitude. The mean  $5\sigma$  limiting magnitude of the reduced images were 25.10 for HeI, 26.28 for  $g$  and 25.36, for  $R$  for an  $2''$  diameter aperture. The limit magnitudes per field are presented in table 2.

If we consider the limit magnitudes reached in the narrow band and in the  $R$  band, we can compute the smaller Ly $\alpha$  EW that we were able to detect on the images. The  $EW_{Ly\alpha}$  is defined as:

$$EW = \frac{F_{Ly\alpha}}{f_{cont}} \quad (1)$$

where  $F_{Ly\alpha}$  is the Ly $\alpha$  flux (in  $\text{erg cm}^{-2} \text{s}^{-1}$  units) and  $f_{cont}$  is the density flux of the continuum (in  $\text{erg cm}^{-2} \text{s}^{-1} \text{\AA}^{-1}$  units). In our case, the broad band  $R$  is containing the continuum and the Ly $\alpha$  line, so, the density flux of the continuum has to be computed using the combined information from the narrow band and the broad band. Following the relations from Yang et al. (2009) we can write it as:

$$f_{cont}^{\lambda} = \frac{F_R - F_{NB}}{\Delta\lambda_R - \Delta\lambda_{NB}} \quad (2)$$

where  $\Delta\lambda_R$  and  $\Delta\lambda_{NB}$  are the FWHM of the R and NB filters respectively. Then the line flux can be written by:

$$F_{Ly\alpha} = F_{NB} - f_{cont}^{\lambda} \Delta\lambda_{NB} \quad (3)$$

If we use the mean  $5\sigma$  limit magnitudes of both NB and R filters, we can compute the limit fluxes, and then  $F_{Ly\alpha,limit}$  and  $f_{cont,limit}^{\lambda}$ . Replacing in the equation (1), we computed the limit EW that we were able to detect, obtaining  $EW_{Ly\alpha,limit} \sim 38\text{\AA}$  (corresponding to an  $EW_{Ly\alpha,RF} = 7.8\text{\AA}$  in rest frame). This means that in our images we were able to detect galaxies with  $EW_{Ly\alpha}$  greater or equal to this value for a detection of  $5\sigma$ . This shows us that the deep of our images is enough to detect LAEs, since they are typically defined as galaxies with  $EW_{Ly\alpha} \gtrsim 20\text{\AA}$ . Using the  $F_{Ly\alpha,limit}$  value, we

also computed the limit of the Ly $\alpha$  luminosity, obtaining  $L_{Ly\alpha,limit} = 1 \times 10^{42} \text{erg s}^{-1}$ .

### 3. LYMAN ALPHA EMITTERS SELECTION

As we mentioned before, the main feature of LAEs is their strong Ly $\alpha$  emission line. For that reason, the technique to identify them is by the detection of a flux excess in the narrow band  $HeI$ , compared with the flux in the continuum traced by our broad band  $R$ , then we expect a blue  $R - HeI$  color. On the other hand, the second broad band is located in order to detect the Lyman break, which can be detected by a red  $g - R$  color. Considering this, a suitable way to select LAEs is studying the  $g - R$ ,  $R - HeI$  color-color diagram.

In the case of LAEs, the selection technique is standard, and the redshift range covered by the filters are very known and easy to calculate. Then, in principle if we adopt the same LAEs selection as previous workers, it is not necessary to calculate a completeness function to compute the clustering, because by construction we should get the same mean number density as them. Even though it is not necessary to compute the completeness of the sample, we use a Monte Carlo simulation described in ? for modeling the LAEs colors in order to have an intuition of the location of them in the color-color diagram.

#### 3.1. Selection Region Choice

To simulate the colors of LAEs, we used a Monte Carlo simulation (?), but with small modifications. For this case we created each spectrum model assigning it a randomly chosen  $EW_{Ly\alpha}$  taken from a different distribution. In this case, we only considered spectra with the Ly $\alpha$  emission line, and then the distribution is built as an exponential function with rest-frame scale length of  $W_0 = -64\text{\AA}$  (Ciardullo et al. 2012).

We took 1000  $EW_{Ly\alpha}$  values from that distribution, but we only considered  $EW_{Ly\alpha,RF} \geq 44\text{\AA}$  since we only select LAEs with this EW limit (as I explain below). The  $EW_{Ly\alpha}$  distribution used in this simulation is shown in Fig. 2.

We also included photometric errors in our simulated colors, but this time assigning to each spectrum a random value for the NB filter, taken from the Ly $\alpha$  luminosity function integrated in the magnitudes limits of our observations. We used the Schechter parameters from Ouchi et al. (2008), who measured the luminosity function for LAEs at  $z \sim 3.7$ , based on a photometric sample of 101 LAEs and a spectroscopic sample of 26 LAEs, with  $EW_{Ly\alpha,RF} \gtrsim 44\text{\AA}$ . The best parameters are given by  $\phi^* = 3.4 \times 10^{-4} \text{Mpc}^{-3}$ ,  $L_{Ly\alpha}^* = -10.2 \times 10^{42} \text{erg s}^{-1} \text{mag}$ , and  $\alpha = -1.5$ .

The results of this color modeling are shown in Fig. 3. We plotted the color of each simulated spectrum as color coded according to the redshift. We overplotted as a continuum curve the mean LAE evolutionary track, where the large filled circle is indicating the position of a LAE at  $z = 3.87$ . The region used to select LAEs is shown as a black dashed line.

The purple, blue, and some of the green points in this plot are LAEs spectra at  $z < 3.87$ , where both, the NB and R band are located over the continuum redward to the Ly $\alpha$  line. Since the continuum of LAEs is nearly flat,

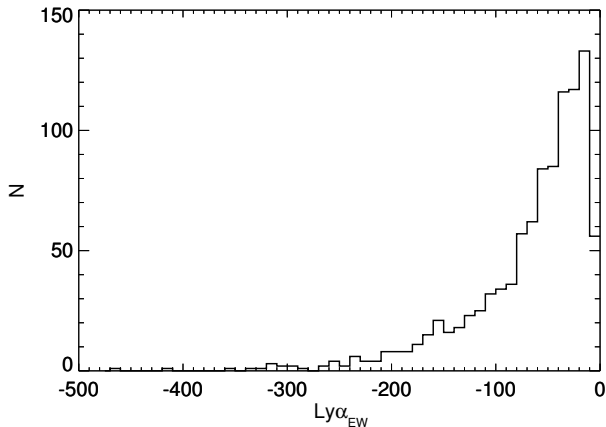


**Figure 2.** Distribution of the  $EW_{Ly\alpha}$  used to create the simulated spectra. Negative values correspond to emission lines.  $EW$  is chosen from an exponential distribution with scale length of  $W_0 = -64\text{\AA}$  (Ciardullo et al. 2012). The mean  $EW_{Ly\alpha}$  of this distribution is  $\sim 90\text{\AA}$ .

the magnitudes of NB and R are similar, then  $R - NB = 0$ . Orange and red points in this plot correspond to LAEs spectra at  $z > 3.87$  and the NB is located blueward to the  $Ly\alpha$  line, where the flux is strongly attenuated by the IGM. The R band is mostly over the continuum, then a red color is expected in the  $R - NB$  axis. When the LAEs is at  $z = 3.87$ , the NB is just over the  $Ly\alpha$  line, then we expected blue colors in  $R - NB$ . The mean evolutionary track shown in the figure, has an  $EW_{Ly\alpha,RF} \sim 90\text{\AA}$ , then the color of any LAE with a more intense  $Ly\alpha$  line will show bluer colors. Furthermore, the  $g$  band is located blueward to the  $Ly\alpha$  line, then we expected a red color in  $g - R$  due to the Lyman break detection. Considering this, we expect the LAEs be located in the upper right region in this diagram. The large scattering of  $z = 3.87$  LAEs colors are due to the photometric errors. When we simulated them, we assigned a noise to the photometry which is greater for fainter magnitudes. The  $z = 3.87$  LAEs are not detected or faintly detected in the  $g$  band, and for those faint magnitudes, the photometric error is big, which produces a large scattering in the  $g - R$  axis of this plot.

We also studied the low- $z$  galaxies location, using the same spectral templates as in section ??, and convolved them with our three filters for different redshift, ranging from 0 to 3. The results are shown in Fig. 4. The locus of the low- $z$  galaxies is well isolated from the  $z = 3.87$  LAEs location, then the contamination is not a problem and this allows us to have a sample with high completeness and purity.

As we explain in the next section, for the clustering measurements, we used the luminosity function of LAEs at  $z = 3.7$  computed by Ouchi et al. (2008), who selected LAEs based on Subaru Suprime-Cam imaging data using the filter set  $B, NB, V$ . This configuration is similar to our configuration  $g, HeI, R$ , and their  $V$  band is also including  $Ly\alpha$ , as our R band do. In order to avoid a redshift selection function computation, we adopted the same color cuts as their work, then this ensures us that our completeness and contamination is the same as their, and we can use directly their luminosity function to

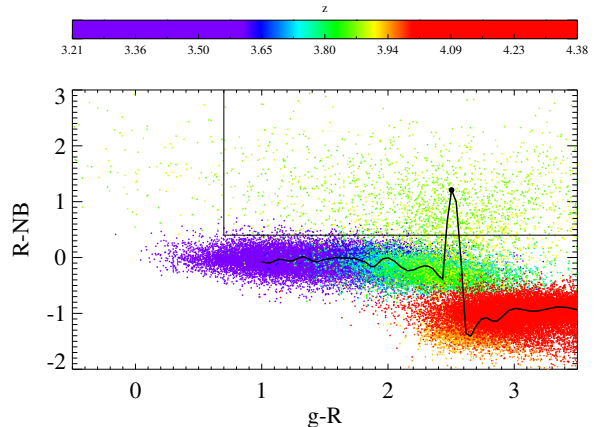


**Figure 3.** Color-color diagram showing the simulated colors of 1000 LAEs spectra, including photometric errors and plotted as redshift color-coded points according to the color bar. The mean LAE evolutionary track is also plotted as a black curve. The filled points over the curve from the left to the right indicate the redshift from 3.3 to 4.1. The larger circle shows the exact position of the mean  $z = 3.87$  LAEs colors and the black dashed line is indicating the LAEs selection region.

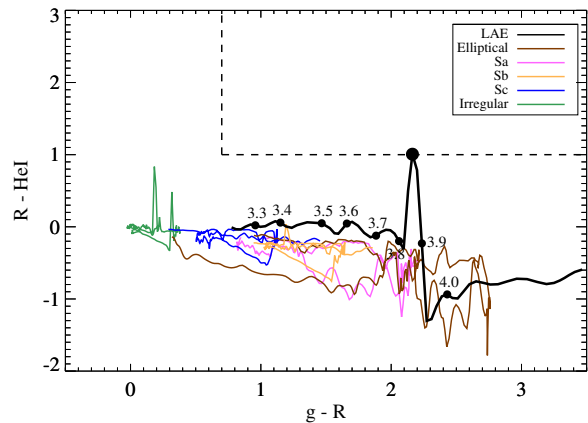


**Figure 4.** Low- $z$  galaxies evolutionary tracks redshifted from  $z = 0$  to  $z = 3$ . We plot as brown, magenta, orange, blue, and red curves the evolutionary track of elliptical, Sa, Sb, Sc, and irregular galaxies respectively. We overplotted the track of LAEs as a red curve. Filled circles over the red curve indicate colors of LAEs from redshift 3.3 to 4.0, and the largest red point indicate the exact position of the color of LAEs at  $z = 3.87$ . We overplotted the selection region as a black dashed line.

compute the number counts in random fields. Our NB limit magnitude is a bit deeper than the used in their study. We reached a median value of  $HeI = 25.1$ , while they reached  $NB = 24.7$ . However, they reached 1.4 mag deeper in their broad band  $V$  in comparison with our R band.

First we defined a lower limit for the detection of the  $Ly\alpha$  line. This limit is basically defining a limit in the  $EW_{Ly\alpha}$  of the detected LAEs. We chose this color cut in  $R - HeI = 1.26$ , which corresponds to an  $EW_{Ly\alpha,RF} \sim 44\text{\AA}$  (computed using equations (2) and (3)). This value is chosen to match with the  $EW_{Ly\alpha,RF}$  used in Ouchi et al. (2008).

The second color cut that we defined is related to the

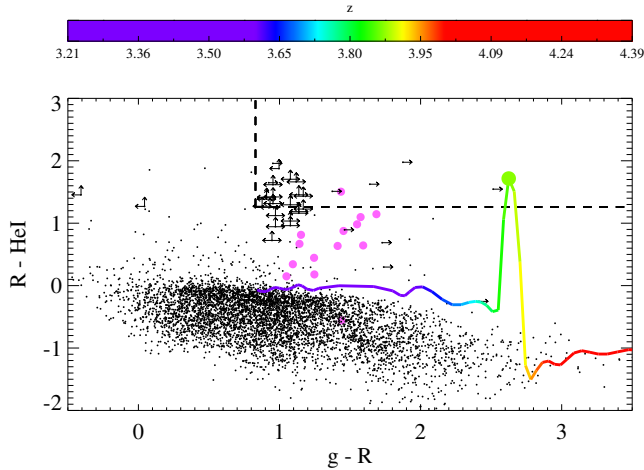


**Figure 5.** Color-color diagram for our 14 stacked QSO fields. Here the evolutionary track showed in Fig. 4 is plotted as redshift color-coded track according to the color bar. The magenta points indicate the color of the QSO in our filters. The magnitudes of cases in which the object was not detected in  $g$  or  $R$  filter at  $2\sigma$  level, were replaced by the corresponding limit magnitude. Those cases are shown with arrows. Cases with no detection on either filter are shown with both arrows. The dashed line is indicating the selection region defined by equations (4) and (5).

detection of the Lyman break, and we chose this cut in  $g - R = 0.83$  which is equivalent to the color cut used in Ouchi et al. (2008), which is given by  $B - V = 0.7$ .

We summarize the color cuts in the equations:

$$R - HeI > 1.26 \quad (4)$$

$$g - R > 0.83 \quad (5)$$

### 3.2. LAEs Sample and Completeness

In each field we selected objects fulfilling the color criteria described in the last section, and we only considered objects detected with  $S/N \geq 5$  in the narrow band filter, in order to ensure the Ly $\alpha$  line detection. The noise is computed in the same way as we described in section ???. We show the color-color diagram of the 14 stacked fields in Fig. 5. We detected 17 LAEs candidates, which correspond to a number density of  $2.88 \times 10^{-2}$  LAEs arcmin $^{-2}$  and  $1.55 \times 10^{-4}$  LAEs Mpc $^{-3}$  (where we have computed the volume of the survey by multiplying the area of the survey by the FWHM of the NB, which is given by  $\Delta z = 0.052$  corresponding to  $\Delta Z = 28.07$  Mpc h $^{-1}$ ). The majority of them are not detected at  $2\sigma$  in either  $R$  and  $g$  filters. In 5 fields we did not detect any LAEs.

Given that our  $R$  imaging is shallower than the  $V$  broad band used in Ouchi et al. (2008), our  $R - HeI$  color cut is excluding 9 possible LAEs candidates which show  $R - HeI$  lower limits (arrow pointing up in the diagram). If we had  $R$  images 1.4 mag deeper, the  $2\sigma$  limit magnitude assigned in  $R$  when there is no detection, would be fainter, and then the lower limits would move to bluer colors, possibly fulfilling our  $R - HeI$  color requirement. Considering this, we compute our clustering including and non including those 9 LAEs in order to study the impact of them in the sample. However, it is needed deeper  $R$  images to confirm they nature. If we include those 9 new LAEs candidates, we obtain a total of 26 LAEs, corresponding to a number density

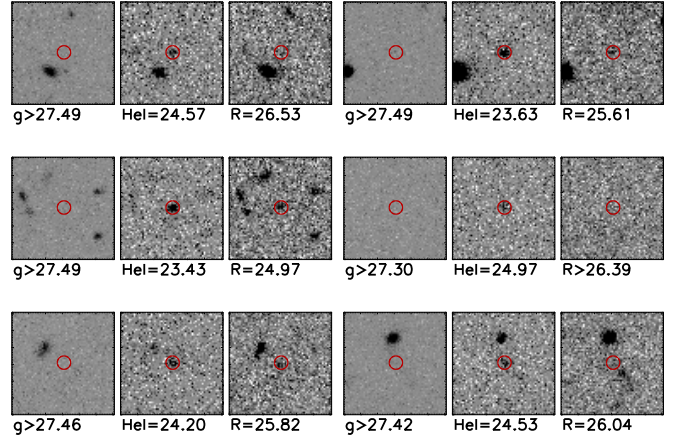


**Figure 6.** Images of some selected LAEs. From left to right we show the  $g$ ,  $HeI$ , and  $R$  images. Each panel is  $15''$  on a side. The red circle shows the position of the detected object, and the size correspond to the region in which the photometry was done ( $2''$  in diameter). The magnitudes are indicated in each panel.

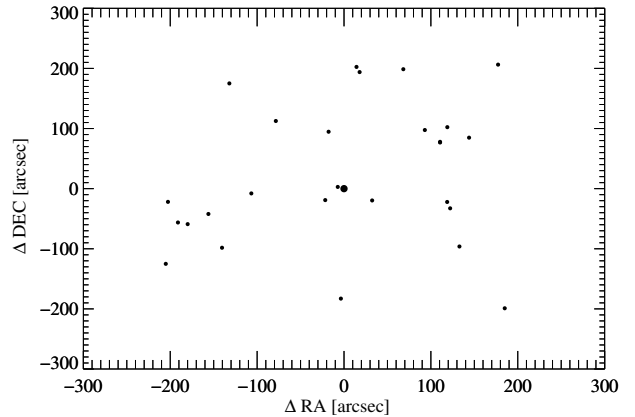


**Figure 7.** The distribution of LAEs around the quasar in the plane of the sky for the stacked 14 fields. The central QSOs is located in 0.0 and is plotted by a large black circle.

of  $4.41 \times 10^{-2}$  LAEs arcmin $^{-2}$  and  $2.37 \times 10^{-4}$  LAEs Mpc $^{-3}$ .

In Table 3 the complete LAEs sample is presented, in Fig. 6 we show some examples of LAEs candidates, and in Fig. 7 we show the distribution of the LAEs for our 14 fields.

Finally, we computed the completeness of the sample for each field by computing the fraction of the simulated spectra in our Monte Carlo which are recovered by our color cuts for each redshift step. We show a median completeness function in Fig. 8. We obtained a completeness of  $\sim 60\%$  at  $3.86 < z < 3.88$  and our color cuts also select LAEs with high completeness (50%) in the redshift range  $3.88 < z < 3.90$  and with a much lower completeness in the range  $3.84 < z < 3.86$ . This corresponds to the fraction of LAEs with  $EW_{Ly\alpha,RF} = 44\text{\AA}$  and magnitude  $HeI \lesssim 25.1$  recovered by our selection region. We computed an effective coverage in redshift as in section ??, and obtained  $\Delta z = 0.027$ , which corresponds to  $\sim 1660$  km s $^{-1}$  at  $z = 3.87$ .

**Table 3**  
LAEs sample. The magnitudes correspond to AB magnitudes measured in a  $2''$  diameter aperture for each filter

ID	RA (J2000)	DEC (J2000)	$r_{\text{GUNN}}$	NB <sub>571</sub>	NB <sub>596</sub>
SDSSJ0040 1	10.0416	17.1033	>26.39	>27.30	25.00
SDSSJ0040 2	10.0318	17.0782	>26.39	>27.30	24.97
SDSSJ0119 1	20.0031	-3.6507	26.53	>27.49	24.57
SDSSJ0119 2	19.9961	-3.7038	25.61	>27.49	23.63
SDSSJ0119 3	19.9449	-3.7202	>26.32	27.31	24.44
SDSSJ0119 4	20.0312	-3.6762	24.97	>27.49	23.43
SDSSJ0119 5	20.0240	-3.6775	>26.32	>27.49	24.88
SDSSJ0119 6*	19.9417	-3.7107	>26.32	>27.49	25.09
SDSSJ0149 1	27.3161	-5.8986	>26.36	>27.48	24.70
SDSSJ1026 1	156.6710	3.4884	>26.32	>27.46	24.87
SDSSJ1026 2*	156.6360	3.4466	>26.32	>27.46	25.16
SDSSJ1026 3*	156.6560	3.5526	>26.32	>27.46	25.14
SDSSJ1044 1	161.0720	9.8350	25.82	>27.46	24.20
SDSSJ1044 2*	161.1660	9.9040	>26.49	>27.46	25.55
SDSSJ1044 3*	161.1110	9.8730	>26.49	>27.46	25.37
SDSSJ1205 1	181.4240	1.7269	26.54	>27.46	24.89
SDSSJ1205 2*	181.4480	1.7262	>26.53	>27.46	25.27
SDSSJ1224 1	186.1170	7.8037	>26.24	>27.32	24.54
SDSSJ1224 2*	186.0490	7.8310	>26.24	>27.32	25.21
SDSSJ1224 3*	186.0640	7.8136	>26.24	>27.32	25.28
SDSSJ1258 1	194.6190	-1.5410	>26.46	>27.42	25.15
SDSSJ1258 2	194.6800	-1.4501	>26.46	>27.42	25.04
SDSSJ1258 3	194.6260	-1.5227	>26.46	>27.42	24.84
SDSSJ1258 4	194.7160	-1.4827	26.04	>27.42	24.53
SDSSJ2250 1*	342.7710	-8.8220	>26.39	>27.34	25.67
SDSSJ2350 1	357.6290	0.4162	>26.33	>27.21	25.06

\* Correspond to 9 LAEs candidates which are not fulfilling our color cut, but they show a lower limit in the  $R - HeI$  color. We would need deeper  $R$  images to confirm those are LAEs.

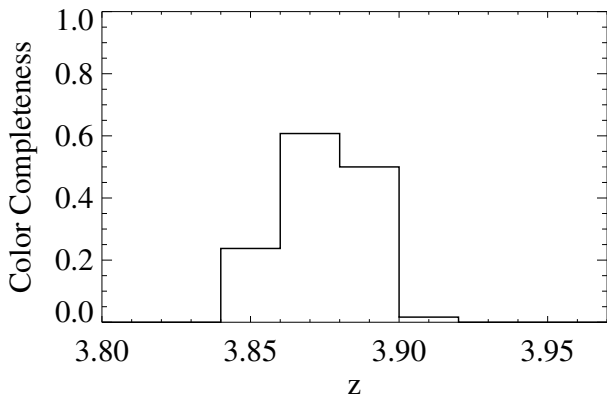


**Figure 8.** Completeness of the LAEs selection. The completeness was determined from 1000 simulated LAE spectra with different EW and, continuum power law and magnitudes. This is calculated by computing the fraction of the simulated spectra, per redshift bin, which was selected by the selection region.

Since we are doing the same selection as Ouchi et al. (2008), we should have the same completeness as them. For their faintest magnitude bin ( $NB = 24.2 - 24.7$ ), they claim a completeness of  $\gtrsim 50\% - 60\%$  which is in agreement with our completeness computation.

Regarding the contamination of the sample, Ouchi et al. (2008) used spectroscopy to estimate a contamination rate. They obtained a contamination within the range of  $0\% - 14\%$  in their LAEs sample. Since we have

the same selection function, we assume the same contamination.

#### 4. CLUSTERING MEASUREMENTS

We computed the expected clustering signal for the QSO-LAE cross-correlation function follow the same procedure as in ?. In this case we compute  $n_G(z, < m_{\text{lim}})$  from the luminosity function of LAEs at  $z = 3.7$  (Ouchi et al. 2008), by integrating it from our limit of Ly $\alpha$  luminosity given by  $L_{\text{Ly}\alpha} \sim 1.0 \times 10^{42} \text{ erg s}^{-1}$  (as computed in the section ??), up to infinity. This  $L_{\text{Ly}\alpha}$  value is computed from the limit magnitudes of  $HeI$  and  $R$  for each field, respectively.

In this case we did not use the completeness function  $C(z)$ , but we assumed  $C(z) = 1$  since the luminosity function was measured with a sample with the same completeness as ours (our LAEs sample have been built in that way). So, here the effective volume of the equation (??) is given by:

$$V_{\text{eff}} = \pi(R_{\text{max}}^2 - R_{\text{min}}^2)\Delta Z \quad (6)$$

with  $\Delta Z$  the comoving distance mapped by our filters, which is computed from the FWHM of the  $HeI$  band. We have  $FWHM = 63.23$ , then  $dz = 0.052$  and  $\Delta Z = 28.07 \text{ Mpc h}^{-1}$ .

For the computation of the  $r_0^{QG}$  value, we used the auto-correlation lengths values for LAEs, given by  $r_0^{GG} = 3.5 \text{ h}^{-1} \text{ cMpc}$  for a fixed  $\gamma = 1.8$  value. This value corresponds to the auto-correlation of LAEs at  $z = 4.86$  (Ouchi et al. 2003), but we assumed that the luminosity function do not show important evolution from

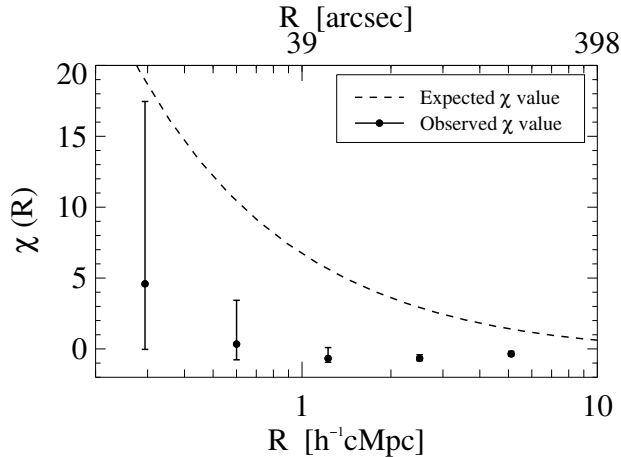


**Figure 9.** QSO-LAE cross-correlation function. The filled circles are showing our measurement with  $1\sigma$  Poisson error bars. The dashed black line shows the theoretical expectation of  $\chi$  for our 14 stacked fields calculated from the QSO and LAEs auto-correlation functions.

**Table 4**  
QSO-LAE Cross-Correlation Function.

R( $h^{-1}$ cMpc)	$\langle QG \rangle$	$\langle QR \rangle$	$\chi$
0.294	1	0.179	$4.593^{+12.864}_{-4.625}$
0.600	1	0.745	$0.342^{+3.086}_{-1.110}$
1.225	1	3.017	$-0.669^{+0.762}_{-0.274}$
2.502	4	12.183	$-0.672^{+0.260}_{-0.157}$
5.107	19	29.353	$-0.353^{+0.185}_{-0.147}$

3.87 to 4.86. The resulting expected  $r_0^{QG}$  value is then  $r_0^{QG} = 8.83 h^{-1} \text{cMpc}$  for a fixed  $\gamma = 1.8$  value, which is a little lower than the expected for the QSO-LBG cross-correlation (?).

We computed the expected value for the QSO-LAE cross-correlation function, which is plotted in Fig. 9 as a dashed line. We also plotted our measured QSO-LAE cross-correlation function as data point, which is computed following the same procedure described in section ???. We have used the sample which include the 9 LAEs candidate with lower limits, located outside of our selection region. The tabulated values of  $\langle QG \rangle$ ,  $\langle QR \rangle$ , and  $\chi$  are shown in Table 4.

As it is seen from Fig. 9 we have got a QSO-LAE cross-correlation measurement which is lower than the expected value. Indeed, for the last 3 bins we obtained negative values for  $\chi$ , which means that the number of LAEs in QSO environments is slightly lower than the number of LAEs expected in random fields.

We explored this result, by computing the cumulative number density of LAEs in our 14 stacked fields (including and not including the 9 candidates outside of our selection region) and comparing it with the number density of LAEs measured by Ouchi et al. (2008) in random fields. We show our results in Fig. 10. The black points are the number density in random fields, and the red points correspond to our measurement without the inclusion of the 9 LAEs. If we include them, we measure

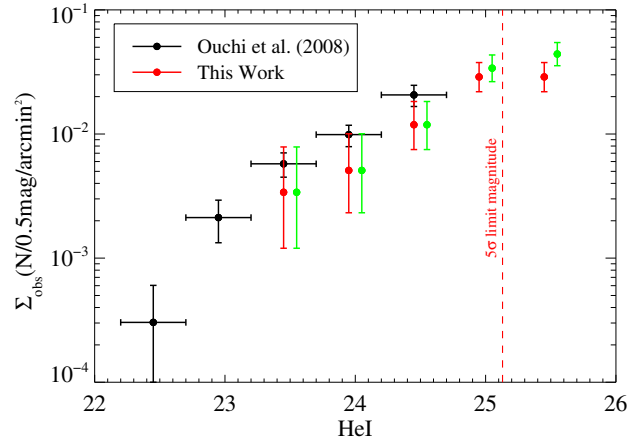


**Figure 10.** Cumulative LAEs number density for our 14 stacked fields, without the inclusion of the 9 LAEs located outside of our selection region (red points). If we include those extra 9 LAEs, they only influence the measurements in the last 2 bins, which is plotted as green points, shifted 0.1 mag for clarity. The black points are the LAEs number density in random fields (Ouchi et al. 2008). The vertical line is indicating the mean  $5\sigma$  limit magnitude of our fields.

the same number density in the first 3 bins, but this variate slightly for the last 2 bins, which is plotted as green points (they were 0.1 mag shifted for clarity). We overplotted as a vertical red line the value corresponding to the mean magnitude of our 14 fields, so, the last bin is not complete for all our fields. The 9 extra LAEs correspond to faint LAEs which are not impacting importantly our results. Regardless of whether we include them or not, our results are consistent the number density in random fields, which suggest that QSOs environments are not especially overdense regions.

Although this result is theoretical unexpected, this is in agreement with some previous results of LAEs searches in QSOs environments at  $z \sim 6$  (Baados et al., 2013; Mazzucchelli et al., 2015 submitted). In their cases, only 1 QSO field was studied, then the no-detection of an enhancement of LAEs, could have been explained by the low number statistics. When only one field is targeted some effect related with cosmic variance can be also affecting the results. In the case of our study, if we analyze our individual fields, we find 4 fields with none LAE, and others with several LAEs. In particular the most overdense field (SDSSJ0119) has 6 LAEs, corresponding to a numerical density of 0.135 LAEs/arcmin<sup>2</sup> (up to magnitude  $HeI = 25.09$ ) which is roughly  $\sim 3$  times higher than the expected number density in random fields. When we stack the signal of our 14 QSO fields, the cosmic variance effect is diluted, as well as the differences in the number density of each field, then we avoid misinterpretation of the results.

There are some possible explanations for our non-overdensity detection. A first one is that the QSO auto-correlation length at  $z \sim 4$  that we used to compute the expected clustering in QSO environments is overestimated. Indeed, some discussion has been done about this topic. The QSO clustering at  $z \sim 4$  measured by Shen et al. (2007) (and used in this thesis) implies dark matter halos masses of  $> 8 \times 10^{12} M_{\odot}$ . However, some simulations (with QSO feedback included in the model)

suggest effective dark matter halos of  $\sim 1.5 \times 10^{12} M_{\odot}$  (Fanidakis et al. 2013), implying that the clustering of QSOs at  $z \sim 4$  could be overestimated. However, note that in that case, we expect that QSO reside in dark matter halos with slightly lower masses, but we still expect a small enhancement of LAEs in QSOs fields over the standard value. We did not detect that enhancement, then we also have to explore other explanations.

Another possibility is that LAEs could be avoiding QSO environments, at least on scales of  $\lesssim 10 \text{Mpc h}^{-1}$ . Some simulations have suggested an extended overdensity in QSOs environments at high redshift, ranging from few to several tens arcmin, and showing variation in the number density across the sky (Overzier et al. 2009; Muldrew et al. 2015). Indeed, some people have found overdensities of galaxies in QSOs environments when they study their environments in large scales of  $3000\text{-}4000 \text{cMpc}^2$  (Utsumi et al. 2010; Morselli et al. 2014). It is necessary to perform an study in wider field-of-view in order to explore this possibility.

Some authors have also suggested that QSO feedback could be suppressing the star formation in the vicinity of the QSO (e.g Francis & Bland-Hawthorn 2004; Bruns et al. 2012). Studies of the ionized regions around  $z \sim 6$  quasars have suggested that this affects at scales of  $\sim 1.5 - 5.2 \text{pMpc}$  (Venemans et al. 2015). In this case we should detect a reduced number of galaxies in this fields. However, other authors claim the opposite effect, suggesting that a luminous QSO could enhance the star formation. In particular, the UV radiation from the QSO could illuminate the neutral gas of nearby galaxies allowing them to fluorescently emit  $\text{Ly}\alpha$  photons (Cantalupo et al. 2012; Borisova et al. 2015). It has been found that possibly this effect could be affecting up to projected distances of  $\lesssim 15 \text{pMpc}$  around  $z \sim 3$  QSOs (Borisova et al. 2015). Note that both mentioned physical processes could affect LAEs differently than LBGs, and then it could be also responsible for the disagreement in the results of LAEs overdensities and LBGs overdensities in QSO fields. A much more deep study of the physical effect of QSOs over nearby galaxies is needed to clarify this picture.

## 5. DISCUSSION

## 6. SUMMARY AND CONCLUSIONS

## REFERENCES

- Appenzeller, I., & Rupprecht, G. 1992, *The Messenger*, 67, 18
- Bertin, E. 2006, in *Astronomical Society of the Pacific Conference Series*, Vol. 351, *Astronomical Data Analysis Software and Systems XV*, ed. C. Gabriel, C. Arviset, D. Ponz, & S. Enrique, 112
- Bertin, E., & Arnouts, S. 1996, *A&AS*, 117, 393
- Bertin, E., Mellier, Y., Radovich, M., et al. 2002, in *Astronomical Society of the Pacific Conference Series*, Vol. 281, *Astronomical Data Analysis Software and Systems XI*, ed. D. A. Bohlender, D. Durand, & T. H. Handley, 228
- Borisova, E., Lilly, S. J., Cantalupo, S., et al. 2015, *ArXiv e-prints*, arXiv:1510.00029
- Bruns, L. R., Wyithe, J. S. B., Bland-Hawthorn, J., & Dijkstra, M. 2012, *MNRAS*, 421, 2543
- Cantalupo, S., Lilly, S. J., & Haehnelt, M. G. 2012, *MNRAS*, 425, 1992
- Cardelli, J. A., Clayton, G. C., & Mathis, J. S. 1989, *ApJ*, 345, 245
- Ciardullo, R., Gronwall, C., Wolf, C., et al. 2012, *ApJ*, 744, 110
- Fanidakis, N., Macciò, A. V., Baugh, C. M., Lacey, C. G., & Frenk, C. S. 2013, *MNRAS*, 436, 315
- Francis, P. J., & Bland-Hawthorn, J. 2004, *MNRAS*, 353, 301
- Fukugita, M., Shimasaku, K., & Ichikawa, T. 1995, *PASP*, 107, 945
- Hennawi, J. F., Prochaska, J. X., Cantalupo, S., & Arrigoni-Battaia, F. 2015, *Science*, 348, 779
- Morselli, L., Mignoli, M., Gilli, R., et al. 2014, *A&A*, 568, A1
- Muldrew, S. I., Hatch, N. A., & Cooke, E. A. 2015, *MNRAS*, 452, 2528
- Oke, J. B. 1974, *ApJS*, 27, 21
- Ouchi, M., Shimasaku, K., Furusawa, H., et al. 2003, *ApJ*, 582, 60
- Ouchi, M., Shimasaku, K., Akiyama, M., et al. 2008, *ApJS*, 176, 301
- Overzier, R. A., Guo, Q., Kauffmann, G., et al. 2009, *MNRAS*, 394, 577
- Patat, F., Moehler, S., O'Brien, K., et al. 2011, *A&A*, 527, A91
- Schlegel, D. J., Finkbeiner, D. P., & Davis, M. 1998, *ApJ*, 500, 525
- Shen, Y., Strauss, M. A., Oguri, M., et al. 2007, *AJ*, 133, 2222
- Stetson, P. B. 2000, *PASP*, 112, 925
- Utsumi, Y., Goto, T., Kashikawa, N., et al. 2010, *ApJ*, 721, 1680
- Venemans, B. P., Bañados, E., Decarli, R., et al. 2015, *ApJ*, 801, L11
- Yang, Y., Zabludoff, A., Tremonti, C., Eisenstein, D., & Davé, R. 2009, *ApJ*, 693, 1579